World Journal of Engineering Research
Print ISSN: 2959-9865
Online ISSN: 2959-9873
DOI: https://doi.org/10.61784/wjer3093

HEALTH-MONITORING-BASED INVESTIGATION OF THERMAL EFFECTS ON DOUBLE-RIBBED PLATE GIRDERS OF CABLE-STAYED BRIDGES

Bo Liu, XiaoQiang Xue*, WenQiang Huang
School of Environment and Civil Engineering, Chengdu University of Technology, Chengdu 610059, Sichuan, China.
**Corresponding Author. XiaoQiang Xue*

Abstract: To investigate the temperature-induced effects on double-ribbed plate girders in cable-stayed bridges, this study leveraged health-monitoring data from the Poyang Lake Bridge. The temperature field distribution was analyzed using ABAQUS, and a full-bridge model was established in Midas/Civil 2021 to examine the mechanical responses of the main girder under overall temperature differences and temperature gradients. The results showed that under the overall temperature drop of 19 °C, the main girder experienced a maximum tensile stress of 6.44 MPa, with extreme vertical and longitudinal displacements of 21.3 mm and 54.6 mm, respectively. Under the overall temperature rise of 21 °C, the maximum compressive stress reached -7.12 MPa, and the extreme vertical and longitudinal displacements were 23.5 mm and 60.4 mm, respectively. Under a positive temperature gradient, the maximum compressive and tensile stresses were -5.47 MPa and 3.52 MPa, respectively, with extreme vertical and longitudinal displacements of 55.1 mm and 26.5 mm. Under a negative temperature gradient, the maximum tensile and compressive stresses were 1.81 MPa and -3.03 MPa, respectively, with extreme vertical and longitudinal displacements of 32.8 mm and 13.5 mm. A comprehensive comparison reveals that the overall temperature difference exerts a more pronounced influence on longitudinal displacement, whereas the vertical temperature gradient, has a more dominant effect on vertical displacement.
Keywords: Health monitoring; Cable-stayed bridge; Double-ribbed plate girder; Temperature field; Temperature gradient

1 INTRODUCTION

The temperature field distribution of bridges is a critical factor influencing structural safety and long-term service performance, particularly for complex spatial structures such as long-span cable-stayed bridges. In recent years, with significant advances in monitoring technologies and computational capabilities, research methodologies have progressively shifted from theoretical simplifications toward a combination of long-term field measurements and high-precision numerical simulations. Long-term health monitoring data have provided essential support for related investigations. Through long-term temperature monitoring of box girders, Kalkan revealed the vertical and transverse temperature gradient, patterns in precast prestressed concrete bridges and proposed an analytical method based on one-dimensional beam theory to calculate their thermal deformations [1]. Using monitoring data combined with planar geometric analysis and finite element simulations, Zhou et al. uncovered distinct temperature-response mechanisms of main girder length and midspan deflection on daily and annual cycles, and established a linear superposition method for estimating temperature effects [2]. Based on one year of monitoring data from the Wangdong Yangtze River Highway Bridge, Zhou et al. analyzed the temperature field distribution of a composite girder cable-stayed bridge, proposed computational models for temperature gradients and component temperature differences, and employed finite element analysis together with the empirical mode decomposition (EMD) method to reveal the decisive influence of cable temperature differences on girder deflection [3]. In the realm of numerical simulation, Chen et al. used a two-dimensional heat transfer model incorporating solar radiation to predict the time-dependent temperature distribution of bridge pylons [4]. Yan et al. developed a three-dimensional computational framework for temperature fields capable of simulating diurnal shading variations [5]. Collectively, these studies have advanced the temperature field analysis of bridges toward greater refinement and practical applicability.

Regarding the temperature effects on large-span structures, extensive work has also been carried out by researchers worldwide. Taking the Youshui Bridge as a case study, Hu et al. employed ANSYS to analyze the solar-induced temperature field and thermal stresses in skewed high piers, and examined the influence of temperature effects on pier forces and bearing reactions [6]. Through a combination of field monitoring and finite element analysis, Hossain et al. studied the temperature gradient, distribution in prestressed concrete continuous girder bridges, verified the applicability of the gradient model specified in the AASHTO code, and evaluated the restraint moments caused by temperature variations as well as their effects on end-cracking of the girder [7]. Using field data from the Sutong Bridge, Gu et al. established a two-dimensional temperature prediction model, proposed vertical and transverse temperature gradient, patterns that account for longitudinal variations, and validated their reasonableness [8].

Despite the substantial achievements of previous studies, research on analytical methods for temperature actions in long-span cable-stayed bridges remains relatively insufficient, and the structural response laws under thermal loads

require further elucidation. To address this gap, the present study, based on the health monitoring system of the Poyang Lake Bridge, conducts a temperature field analysis and temperature-effect investigation of the double-ribbed plate girder. The aim is to reveal its spatiotemporal evolution characteristics, clarify the actual thermal-mechanical behavior under complex environmental conditions, and thereby provide a basis for optimizing the estimation of thermal stresses, preventing cracking of the main girder, and rationally designing bearings.

2 ENGINEERING BACKGROUND AND MONITORING DATA ANALYSIS

2.1 Engineering Background

This study is conducted on the Poyang Lake Bridge, a prestressed concrete cable-stayed bridge with twin towers and twin cable planes. The bridge has a span arrangement of 65 m + 123 m + 318 m + 130 m, as illustrated in Figure 1(a). The main girder adopts a double-ribbed plate section (Figure 1b), with a girder depth of 2.6 m, a top slab thickness of 0.28 m, a deck width of 27.5 m, and a diaphragm spacing of 8 m. The towers are of H-shaped design, and the lower crossbeam of the main tower forms a semi-floating system. A total of 76 pairs of stay cables are arranged, with 22 pairs on each side of the taller tower and 16 pairs on each side of the shorter tower. The standard cable spacing along the main girder is 8 m, except for the backstay cables at the short-tower side span. The structural health monitoring system of the bridge covers wind loads, ambient temperature and humidity, structural temperature and stress, global deformation, cable forces, vibration, bearing and expansion joint movements, among other parameters [9]. A total of 135 sensors are installed across the bridge, including 34 temperature sensors, of which 30 are located on the main girder cross-section. The detailed sensor layout is shown in Figure 1.

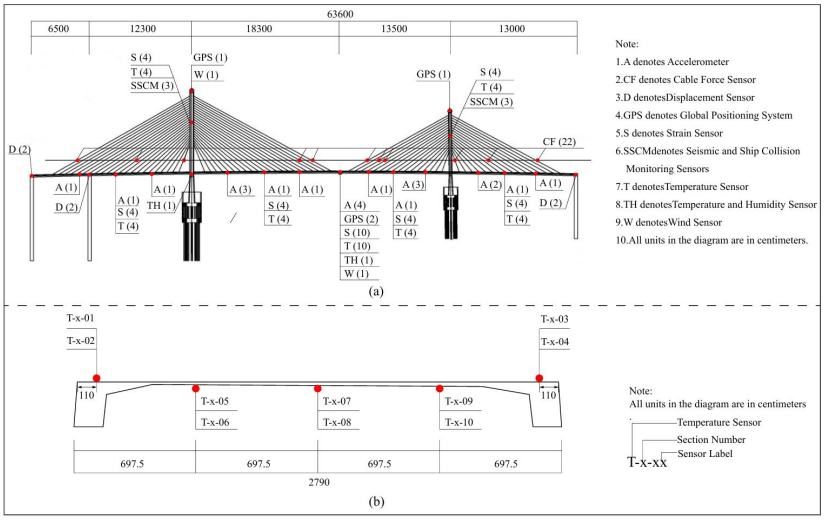

Figure 1 Structural configuration and sensor layout of the Poyang Lake Bridge

2.2 Monitoring Data Analysis

2.2.1 Ambient air temperature

Based on the ambient air temperature data recorded in 2016, the mean temperature on the downstream side of the midspan deck was 19.50 °C, with a maximum of 39.29 °C and a minimum of 0.55 °C. At the downstream side of the deck near the taller tower, the corresponding values were 19.67 °C, 40.67 °C, and 1.02 °C, respectively. The highest temperature occurred on 31 July, and the lowest on 24 November. The temperature trends at the two locations were generally consistent, indicating a uniform thermal environment around the bridge site. Moreover, the annual temperature range remained within the design limits of the bridge, exerting no appreciable influence on its structural performance.

2.2.2 Structural temperature

According to the structural temperature data collected in 2016, the annual average temperature of the Poyang Lake Bridge ranged from 18.76 °C to 22.31 °C. The average temperature on the downstream side was approximately 20 °C, whereas that on the upstream side reached about 22 °C, a difference mainly attributable to the upstream side receiving direct solar radiation (sunny side) and the downstream side being shaded (shady side). The highest structural temperature of 57.87 °C was recorded on the upstream side of the deck at the midspan of the main span, while the lowest structural temperature of 1.02 °C occurred at the bottom surface of the midspan. Temperatures measured at quarter-span locations (T-01-01 and T-01-02) were higher than those at midspan (T-01-03 and T-01-04), indicating a certain degree of longitudinal temperature variation along the structure. Furthermore, sensors at different transverse positions within the same cross-section exhibited consistent temperature differences, revealing a stable transverse temperature gradient. Overall, all measured temperature values remained within the structural design limits. Nevertheless, the observed temperature gradients and longitudinal temperature differences are directly responsible for the non-uniform thermal deformation and secondary internal forces in the main girder, thereby providing a critical basis

for subsequent evaluation of thermal effects on structural internal forces and displacements.

2.2.3 Temperature gradient

The Poyang Lake Bridge is a mass concrete structure. Under solar radiation, the sunny side undergoes rapid temperature rise, whereas the shady side warms up more slowly, resulting in significant temperature differences between the top and bottom slabs as well as between the upstream and downstream sides, thereby inducing considerable secondary internal forces. The factors affecting the temperature distribution of bridges mainly include bridge orientation, geographic location, intensity and duration of solar radiation, among others [10]. Owing to the low thermal conductivity of the concrete girder, a pronounced temperature gradient, readily develops between the upstream and downstream sides of the cross-section under solar exposure, and the resulting secondary internal forces cannot be overlooked. As shown in Table 1, the temperature gradient, at the main-span midspan in 2016 varied between -13.48 °C and 17.18 °C. The monitoring data indicate that the temperature gradient, is positive under daytime solar conditions and increases with the intensity of solar radiation. The minimum temperature gradient, typically occurs around 8:00 a.m., after which it gradually rises as solar radiation intensifies.

Table 1 Statistics of Temperature Gradients at the Midspan of the Main Span in 2016

Month	Maximum (ºC)	Minimum (ºC)	Mean (ºC)
2	11.46	-1.82	1.84
3	12.36	-5.42	1.11
4	4.07	-9.66	-0.50
5	11.90	-2.16	-1.45
6	2.29	-13.48	-1.78
7	11.59	-7.45	-0.40
8	16.61	-12.77	2.30
9	17.18	-3.11	2.40
10	12.64	-2.84	1.32
11	12.53	-0.07	2.43
12	10.75	0.47	3.54

3 FINITE ELEMENT MODEL

3.1 ABAQUS Finite Element Model

3.1.1 Thermal boundary conditions of the model

The thermal boundary conditions of the model mainly consist of three components: solar radiation, convective heat transfer, and radiative heat transfer, as illustrated in Figure 2. Solar radiation can be further decomposed into direct solar radiation, diffuse atmospheric radiation, and ground-reflected radiation [11,12]. Convective heat transfer generally refers to the heat exchange between the structure and the surrounding air, which occurs when airflow passes over the structural surface and a temperature difference exists between the surface and the ambient air. Radiative heat transfer denotes the emission of radiant energy from the structure to the external environment in the form of electromagnetic waves. The convective heat transfer coefficient (h_c) can be calculated using the following equation:

$$h_c=4.0V+5.99 \quad (1)$$

where V represents the wind speed. Based on the wind speed statistics from the 2016 health monitoring data, a wind speed of V=4.0 m·s^{-1}was adopted, and the convective heat transfer coefficient was calculated using Equation (1) as h_c=21.99 W·(m·°C)$^{-1}$. As the influence of radiative heat transfer on component temperatures is smaller than that of the two aforementioned mechanisms, thermal radiation was equivalently applied as convective heat transfer in the loading procedure [13].

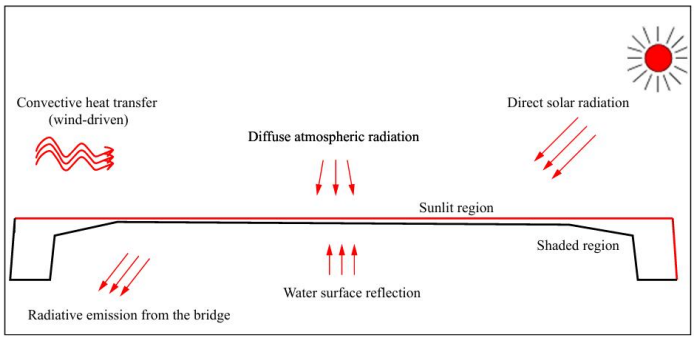

Figure 2 Thermal Boundary Conditions of the Structural Temperature Field

According to the 2016 health monitoring data, the summer air temperature peaked in July, with 31 July being the hottest day. Considering the bridge's geographic location (117° E, 29° N) and its east–west orientation, the solar radiation intensity on each structural component on that day was calculated following the method of Ref. [14]; the results are presented in Figure 3. Figures 3(a) and 3(b) show the diurnal variations of reflected and diffuse radiation, respectively, both of which were considerably lower than direct radiation and exhibited a unimodal trend of first increasing and then decreasing. As illustrated in Figure 3(c), the direct solar radiation on the upstream and downstream main ribs displayed a nearly symmetrical "V"-shaped distribution with opposite trends. During sunrise and sunset, the direct radiation on the main ribs was higher than that on the top slab. As the solar altitude angle increased, the direct radiation on the top slab gradually intensified, reaching its peak at noon and significantly exceeding that on the main ribs. The peak direct radiation intensity on the upstream main rib reached 826.2 $W \cdot m^{-2}$, whereas the downstream main rib received only diffuse and reflected radiation amounting to 194.3 $W \cdot m^{-2}$. This order-of-magnitude difference is the fundamental cause of the transverse temperature difference of up to 5.7 °C. Figure 3(d) presents the total solar radiation intensity. Owing to the east–west orientation of the bridge, the downstream main rib received no direct sunlight, whereas the upstream main rib did, resulting in a substantially higher total radiation on the upstream side than on the downstream side. The total radiation on the top slab and bottom surface reached their maxima around noon, while the trends on the upstream and downstream main ribs were opposite to each other.

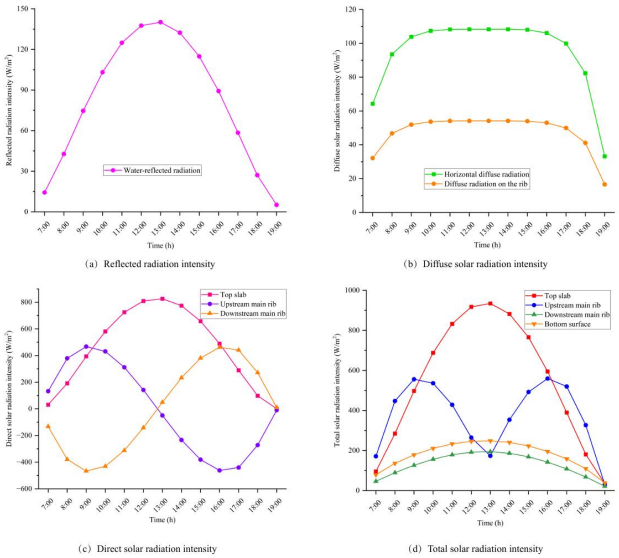

Figure 3 Solar Radiation Intensity on the Double-ribbed Plate Girder

3.1.2 Parameter settings

The convective heat transfer coefficient was taken as h_c=21.99 $W \cdot (m \cdot °C)^{-1}$. Based on historical weather forecasts and monitoring data, the ambient temperature range on the hottest day in July was selected as 29-39 °C to represent the most unfavorable condition. The water surface reflectivity was set to 0.15. The day of the year was taken as 213, with 1 January as the starting point. The bridge's geographic location was set at 117° E, 29° N, and its orientation was taken as east–west according to the actual alignment. The main material parameters are listed in Table 2.

Table 2 Main Material Parameters

Material property	Value
Strength grade	C55
Density	2500 kg·m-³
Specific heat capacity	860 $J \cdot (kg \cdot °C)^{-1}$
Thermal conductivity	1.5 $W \cdot (m \cdot °C)^{-1}$
Coefficient of thermal expansion	1×10^{-5} $°C^{-1}$
Thermal radiation absorptivity	0.6
Elastic modulus	35.5GPa

3.1.3 Model development

A three-dimensional finite element model of the double-ribbed plate girder was established using ABAQUS to simulate its temperature field distribution, as shown in Figure 4. The main girder was discretized using linear hexahedral heat transfer elements, with a total of 98,124 elements to ensure the fidelity of the simulated temperature transfer. The model comprehensively incorporates three forms of heat exchange between the double-ribbed plate girder and the external environment: convective heat transfer, thermal radiation, and solar radiation. Convective heat transfer was implemented by defining a film coefficient and an ambient temperature as surface heat exchange conditions, with

the convective heat transfer coefficient set to 21.99 $W\cdot(m\cdot°C)^{-1}$. For thermal radiation, the ambient radiation temperature was taken as the time history of the measured air temperature on that day (29–39 °C), the surface emissivity of the material was set to $\varepsilon = 0.92$, and the Boltzmann constant was taken as $\sigma = 5.67 \times 10^{-8}\ W\cdot(m^2\cdot K^4)^{-1}$. Solar radiation was applied as a surface heat flux on all exposed surfaces, including the top slab, upstream and downstream main ribs, and the bottom surface.

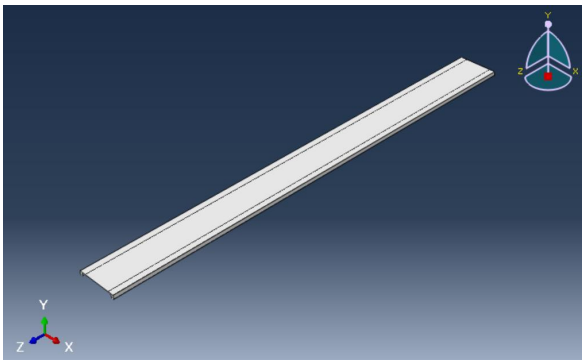

Figure 4 ABAQUS Finite Element Model

Based on field monitoring data, the initial temperature of the model was set to 34 °C, corresponding to the measured average deck temperature at 00:00 on 31 July, ensuring that the starting point of the transient analysis was consistent with the actual thermal state. A total of 25 analysis steps were set: the first step had a duration of 86,400 s to eliminate the influence of initial transient disturbances on the temperature field, and the subsequent 24 steps each had a duration of 3,600 s to precisely capture the evolution of the temperature gradient, over a diurnal cycle.

3.2 ABAQUS Finite Element Model

A three-dimensional finite element model of the unequal-height twin-tower cable-stayed bridge was established using Midas/Civil 2021, as shown in Figure 5. The material parameters of the various structural components are listed in Table 3. The main girder and the towers were simulated using beam elements, whereas the stay cables were modelled as truss elements. The entire bridge model consisted of 408 nodes and 407 elements. The main girder was divided into 79 elements, numbered sequentially from left to right as elements 1-9, 407, and 10-78, with element 407 corresponding to the auxiliary pier location. The taller tower was located at node 24, and the shorter tower at node 63. The stay cables were arranged in a fan-shaped dense cable system. The taller and shorter towers formed a mother-and-child twin-tower configuration, with 22 pairs of stay cables on each cable plane of the taller tower and 16 pairs on each plane of the shorter tower, giving a total of 76 pairs for the entire bridge. Regarding connections and boundary conditions, the anchorage between the stay cables and the tower or main girder was simulated as rigid connections. Both the taller and shorter towers were fixed to the piers and girders (tower–pier–girder consolidation). Longitudinally sliding bearings were provided at the auxiliary pier adjacent to the taller tower [15,16].

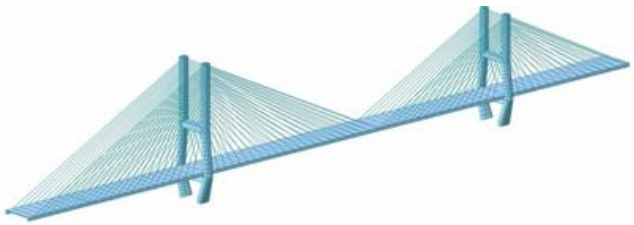

Figure 5 MIDAS Finite Element Model

Table 3 Finite Element Model Material Parameters

Structural parts	Material	Elastic modulus (GPa)	Poisson'sratio	Bulk density ($kN\cdot m^{-3}$)	Coefficient of linear thermal expansion ($°C^{-1}$)
Main beam	C55	35.5	0.2	25	1.0×10^{-5}
Upper tower column	C50	34.5	0.2	25	1.0×10^{-5}
Middle tower column	C40	32.5	0.2	25	1.0×10^{-5}
Lower tower	C40	32.5	0.2	25	1.0×10^{-5}

Structural parts	Material	Elastic modulus (GPa)	Poisson'sratio	Bulk density ($kN \cdot m^{-3}$)	Coefficient of linear thermal expansion ($℃^{-1}$)
column					
Stay cable	ASTMA416-270(Low)	196.5	0.3	77.09	1.17×10^{-5}

Based on the temperature field analysis results, a three-dimensional finite element model was established in Midas to systematically investigate the temperature effects on the main girder from two aspects: overall temperature difference and vertical temperature gradient. According to the most unfavorable air temperatures measured on the Poyang Lake Bridge in 2016, a reference temperature of 20 °C was adopted, and uniform temperature loads corresponding to an overall temperature drop of 19 °C and an overall temperature rise of 21 °C were applied. For the vertical temperature gradient, a positive gradient of T_1=42.5℃and T_2=22.2℃ and a negative gradient of T_1=14.1℃and T_2=19.7℃, were prescribed.

4 TEMPERATURE FIELD ANALYSIS

4.1 Temperature Distribution Characteristics

Using the ABAQUS finite element software, this study simulated the temperature field of the double-ribbed plate girder based on field measurements and monitoring data, taking into account the combined effects of solar radiation and air temperature variations. Figure 6 presents the temperature variation curves over the full day of 31 July. The top slab exhibited the highest temperature, reaching a maximum of 62.55 °C. Owing to the east–west orientation of the bridge, the upstream main rib received direct solar radiation during daytime and thus became significantly hotter than the downstream main rib. Conversely, the downstream main rib, being in the shade, registered temperatures even lower than those of the bottom surface during sunshine hours. Over the 24-hour temperature cycle, the differences among various structural components were small during the nocturnal cooling phase but increased markedly during the daytime heating phase. Under the combined influence of solar radiation and bridge orientation, the peak temperatures of different surfaces occurred at different times: the overall maximum temperature appeared at 15:00, at which the top slab also reached its peak; the bottom surface peaked at 16:00; the upstream main rib peaked at 18:00; and the downstream main rib peaked at 17:00. These differences in peak timing are primarily attributable to the thermal inertia of the concrete material.

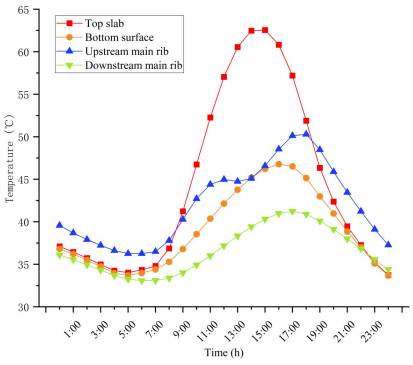

Figure 6 Temperature Variation Curves of Various Main Girder Components on 31 July

To visualize the temperature distribution characteristics of the double-ribbed plate girder, Figures 7 and 8 present the temperature field contours of the main girder over a 24-hour period. As shown in these figures, the transverse temperature distribution of the main girder was generally uniform and followed a consistent pattern. Under solar radiation, heat was transferred from the top surface downward and simultaneously from the mid-span towards the lateral ribs on both sides. The structural surfaces responded rapidly to temperature variations, whereas the internal temperature fluctuated more gently, resulting in pronounced vertical and transverse temperature gradients. The peak temperature of the main girder occurred at 15:00, and the minimum temperature appeared at 6:00, exhibiting a notable thermal lag. From the overall temperature contours, it can be seen that during the daytime heating phase, solar radiation directly impinged on the top surface and the upstream main rib. Owing to the downstream main rib being in the shade, its temperature remained consistently lower than that of the upstream side. During this period, the deck temperature was highest at the mid-width and gradually decreased towards both sides, displaying a "high in the middle, low at the edges" distribution pattern. This pattern arises because heat is transferred downward at the girder ends, causing the surfaces of the double ribs to be cooler than the mid-deck region. Conversely, during the nocturnal cooling phase, the temperature distribution reversed to a "low in the middle, high at the edges" trend.

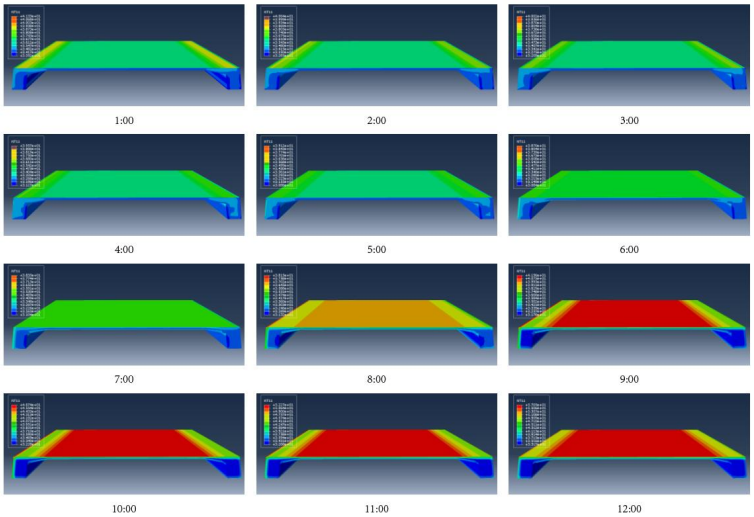

Figure 7 Overall Temperature Distribution Contours (01:00–12:00)

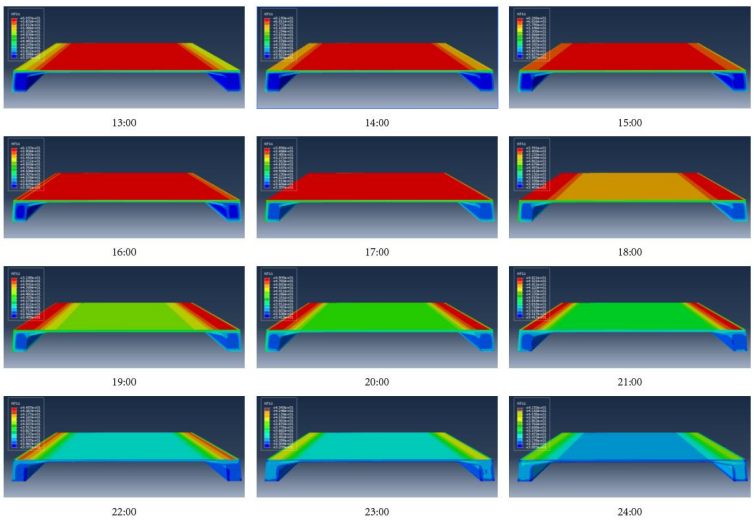

Figure 8 Overall Temperature Distribution Contours (13:00–24:00)

4.2 Vertical Temperature Field Distribution of the Main Girder Section

Figure 9 presents the vertical temperature gradient curves inside the rib section of the main girder. As shown in Figure 9, the vertical temperature distribution within the double-ribbed plate girder of the Poyang Lake Bridge was consistently non-uniform, exhibiting a distinct positive and inverse "C-shaped" pattern, indicating a pronounced temperature gradient. Owing to the low thermal conductivity of concrete, a significant thermal lag was observed in heat transfer. During the nocturnal cooling phase, the temperature followed an inverse "C-shaped" distribution, with the lowest temperature occurring at the bottom surface of the girder. The maximum temperature difference of approximately 3.3 °C occurred around 6:00 a.m. In contrast, during the daytime heating phase, the distribution transformed into a positive "C-shape", with the lowest temperature located at the mid-depth of the section, and the maximum temperature difference reached 22.7 °C around 4:00 p.m. The surface temperature of the rib peaked at 4:00 p.m. and bottomed out at 5:00 a.m. Within the range of 0.4–0.45 m from the top of the girder, the temperature varied sharply, whereas the temperature gradient was relatively small in the 0.4–0.8 m region, where the temperature remained largely stable. Under the influence of diffuse and reflected radiation during the day, the bottom surface temperature was higher than that at the mid-depth; during the nocturnal cooling process, it gradually dropped below the mid-depth temperature. Overall, the distribution followed the pattern of "low in the middle and high at both ends during heating, and high in the middle and low at both ends during cooling". Figure 10 shows the vertical temperature contour of the main girder, which clearly illustrates the vertical thermal stratification of the double-ribbed plate girder: during the early morning and nighttime, the temperature at the mid-depth of the girder was higher than that at the top and bottom surfaces. Under solar radiation, the structural surface warmed up rapidly, and heat was transferred downward, whereas the internal temperature changed more gently. This distribution characteristic is consistent with the temperature pattern observed inside the girder ribs.

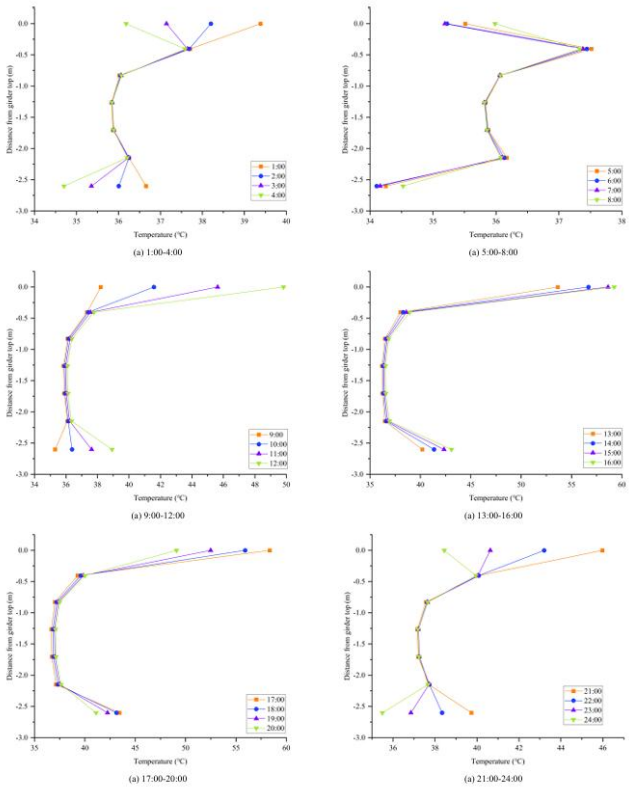

Figure 9 Vertical Temperature Distribution in the Girder Rib Cross-section

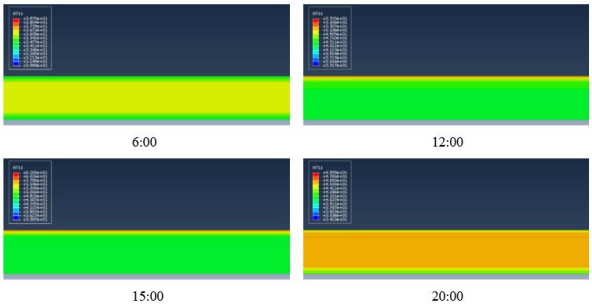

Figure 10 Vertical Temperature Distribution Contours

4.3 Transverse Temperature Field Distribution of the Main Girder Section

Figure 11(a) shows equidistant points H1-H7 arranged from the upstream to the downstream side at the midspan of the main girder, and Figure 11(b) presents the 24-hour temperature variation curves at these transverse locations on the surface of the double-ribbed plate girder. As can be seen from Figure 11(b), the temperature on the upstream side (H7) was significantly higher than that on the downstream side (H1), with a substantial temperature difference between the two sides, indicating that the structure also exhibits a pronounced transverse temperature gradient.

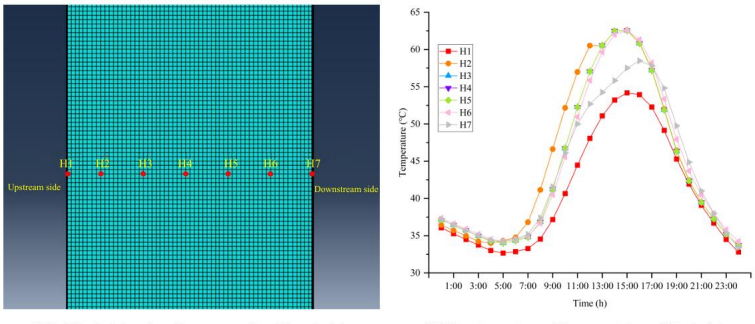

(a) Equidistant points on the midspan cross-section of the main girder (b) 24-hour temperature variation curves at the equidistant points

Figure 11 Diurnal Temperature Variations at Transverse Locations on the Main Girder

Figure 12 presents the transverse temperature gradient curves of the main girder during daylight hours. Owing to solar

radiation, a pronounced transverse temperature difference developed across the main girder. The temperature difference between the upstream and downstream sides reached its maximum of 5.7 °C at 18:00, exhibiting a distribution pattern where the upstream side was consistently warmer than the downstream side. During the day, the temperature gradient was generally positive and increased with solar radiation intensity, with the minimum typically occurring around 8:00 a.m. Although the average deck gradient in July was negative, the upstream side remained generally warmer than the downstream side, consistent with the actual condition of sunny versus shaded sides.

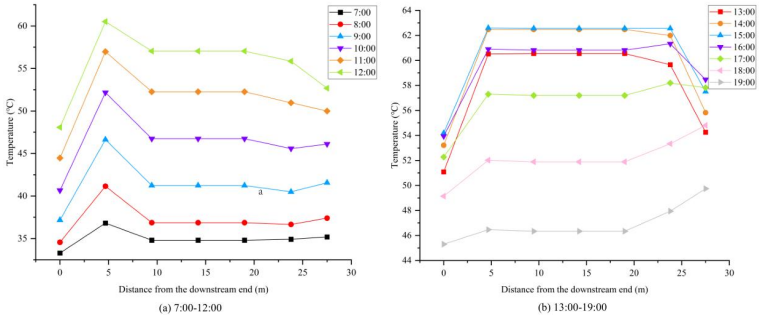

Figure 12 Transverse Temperature Gradient Curves of the Main Girder during Daylight Hours

5 TEMPERATURE EFFECTS ON THE MAIN GIRDER

5.1 Stress Analysis of the Main Girder

Figures 13(a) and 13(b) show the stress distributions on the top and bottom flanges of the main girder under the overall temperature rise of 21 °C and the overall temperature drop of 19 °C, respectively. Under the overall temperature drop of 19 °C, the combined stresses on both the top and bottom flanges were predominantly tensile. The maximum tensile stress reached 2.80 MPa on the top flange and 6.44 MPa on the bottom flange. Compressive stresses also appeared in some cross- sections, with maximum values of -0.75 MPa on the top flange and-3.60 MPa on the bottom flange. Under the overall temperature rise of 21 °C, the stress state changed markedly: the combined stresses on both flanges were mainly compressive, with maxima of -3.09 MPa on the top flange and -7.12 MPa on the bottom flange. Tensile stresses still existed in some sections, reaching up to 0.83 MPa on the top flange and 3.97 MPa on the bottom flange. The stress distributions under vertical temperature gradients are shown in Figures 13(c) and 13(d). Under a positive temperature gradient, the combined stresses on the top flange were entirely compressive, with a maximum of -5.47 MPa. Under a negative temperature gradient, except for a local region near the auxiliary pier where compressive stresses appeared, the top flange was under tension, with a maximum tensile stress of 1.81 MPa. Notably, the presence of the auxiliary pier significantly altered the local stress state, reducing tensile stresses or even converting them into compressive stresses in that region. Under a positive temperature gradient, the bottom flange stresses exhibited a distinct regional pattern: both side spans were under tension, with a maximum tensile stress of 3.52 MPa, whereas the taller- tower zone, the mid- span of the main span, and the vicinity of the shorter tower experienced compressive stresses, with a maximum of -1.20 MPa. The stress curves showed pronounced inflections at the locations of the taller and shorter towers. Under a negative temperature gradient, the side spans on both sides of the taller and shorter towers were predominantly under compression, with a maximum compressive stress of -3.03 MPa, whereas the main span was entirely under tension, with a maximum tensile stress of 1.58 MPa. Compared with the positive temperature gradient case, the inflections in the stress curve at the taller and shorter towers were substantially reduced under the negative temperature gradient.

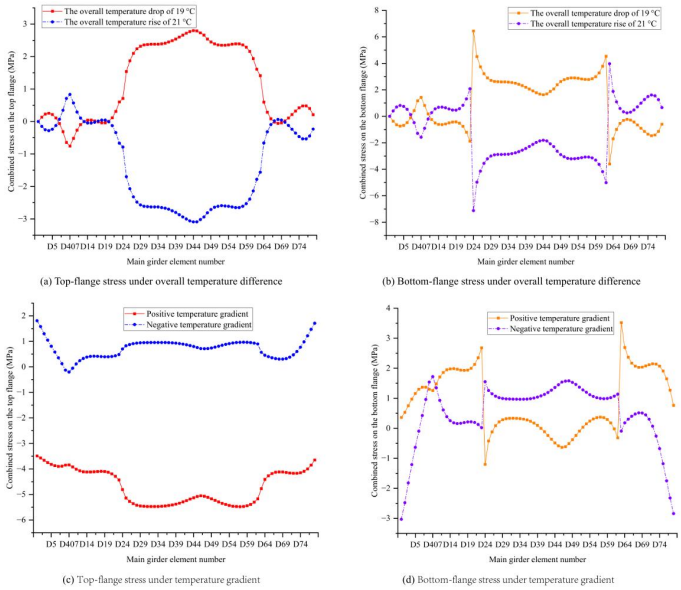

Figure 13 Stresses in the Main Girder

5.2 Displacement Analysis of the Main Girder

Overall temperature variation not only induces stress in the main girder but also causes its displacement. Figure 14 presents the vertical and longitudinal displacements of the main girder under four cases: Overall temperature rise of 21 °C, Overall temperature drop of 19 °C, Positive temperature gradient, and Negative temperature gradient.

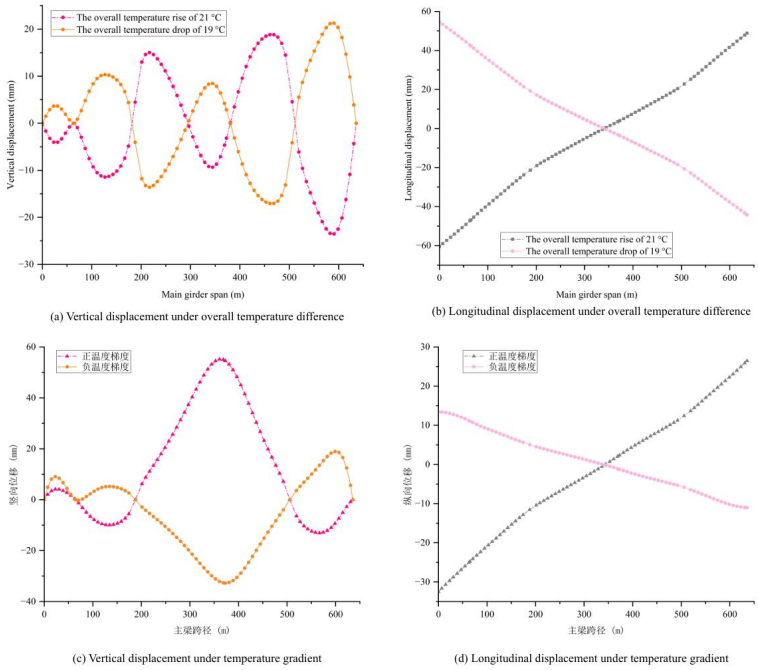

Figure 14 Vertical and Longitudinal Displacements of the Main Girder

As shown in Figures 14(a) and 14(c), under the overall temperature drop of 19 °C, both the left side span of the taller tower and the side span of the shorter tower underwent upward camber, with maximum values of 10.3 mm on the taller-tower side and 21.3 mm on the shorter-tower side. In the main span, both upward camber (maximum 8.5 mm) and downward deflection (maximum -17.0 mm) occurred. Under the overall temperature rise of 21 °C, the displacement trends were opposite: the left side span of the taller tower and the side span of the shorter tower experienced downward deflection, with maxima of -11.4 mm and -23.5 mm, respectively, while the main span exhibited upward camber up to 18.8 mm and downward deflection down to -9.4 mm. Under a positive temperature gradient, upward camber occurred in the left side span of the auxiliary pier and in the main span between the taller and shorter towers, whereas downward deflection occurred in the span between the auxiliary pier and the taller tower as well as in the right side span of the shorter tower. Across the entire bridge, the maximum upward camber was 55.1 mm, and the maximum downward deflection was -13.1 mm. Under a negative temperature gradient, upward camber occurred in the two spans to the left of the taller tower and in the right side span of the shorter tower, reaching a maximum of 19.0 mm on the shorter-tower

side, while the main span between the taller and shorter towers experienced downward deflection with a maximum of 32.8 mm. Figures 14(b) and 14(d) show that under all four cases, the maximum longitudinal displacement of the main girder occurred at the girder ends, decreased progressively from the ends towards midspan, and the displacement directions at the two ends were opposite. Under the overall temperature drop of 19 °C, the maximum longitudinal displacement at the left end (taller-tower side) was 54.6 mm, and at the right end (shorter-tower side) was -44.2 mm. Under the overall temperature rise of 21 °C, the corresponding values were -60.4 mm (taller-tower side) and 48.9 mm (shorter-tower side). Under the negative temperature gradient, the maximum longitudinal displacements were 13.5 mm (taller-tower side) and -11.0 mm (shorter-tower side). Under the positive temperature gradient, they were -32.5 mm (taller-tower side) and 26.5 mm (shorter-tower side). Compared with the case of overall temperature rise of 21 °C, the influence of the positive temperature gradient on the longitudinal deformation of the main girder followed the same trend, whereas the effects of the overall temperature drop of 19 °C and the negative temperature gradient exhibited opposite trends.

A comprehensive comparison of the displacement responses under the four cases reveals that the overall temperature difference exerts a more pronounced influence on the longitudinal displacement of the main girder, whereas the vertical temperature gradient has a more dominant effect on the vertical displacement. The effect of the overall temperature drop of 19 °C on girder displacements is slightly weaker than that of the overall temperature rise of 21 °C. Moreover, the positive temperature gradient induces substantially larger displacements than the negative temperature gradient.

6 CONCLUSION

In this study, the temperature field distribution of the double-ribbed plate girder over a 24-hour period was first simulated using ABAQUS. Subsequently, the mechanical responses of the main girder under overall temperature differences and thermal gradients were analyzed with Midas/Civil 2021. The following conclusions can be drawn:

(1) During daytime, the highest temperature of the double-ribbed plate girder in the unequal-height twin-tower cable-stayed bridge occurs at the mid-width of the deck and propagates laterally towards both sides, exhibiting a “high in the middle, low at the edges” distribution pattern. At night during cooling, the pattern reverses to “low in the middle, high at the edges”.

(2) The overall temperature difference exerts a more pronounced influence on the longitudinal displacement of the main girder, whereas the vertical temperature gradient has a more dominant effect on the vertical displacement. The influence of the overall temperature drop of 19 °C on girder displacements is slightly weaker than that of the overall temperature rise of 21 °C. Moreover, the positive temperature gradient induces substantially larger displacements than the negative temperature gradient.

(3) Under the positive temperature gradient, both the extreme stresses and the displacements of the main girder are generally larger than those under the negative temperature gradient. Furthermore, the inflection amplitude of the stress curve at the tower locations is also more significant, indicating that the structural response is more sensitive to the positive temperature gradient.

COMPETING INTERESTS

The authors have no relevant financial or non-financial interests to disclose.

REFERENCES

[1] Lee Jong-Han, Kalkan Ilker. Analysis of thermal environmental effects on precast, prestressed concrete bridge girders: temperature differentials and thermal deformations. Advances in Structural Engineering, 2012, 15(3): 447-459. DOI: 10.1260/1369-4332.15.3.447.

[2] Zhou Yi, Sun Limin. Insights into temperature effects on structural deformation of a cable-stayed bridge based on structural health monitoring. Structural Health Monitoring, 2019, 18(3): 778-791. DOI: 10.1177/1475921718773954.

[3] Zhou Hao, Yi Yuelin, Ye Zhongtao, et al. Temperature field and thermal effect analysis of long-span composite girder cable-stayed bridge. Bridge Construction, 2020, 50(5): 50-55.

[4] Chen Bo, Guo Weihua, Song Chunfang, et al. Numerical assessment on time-varying temperature field of bridge tower under solar radiation. Applied Mechanics and Materials, 2012, 1975(204-208): 2236-2239. DOI: 10.4028/www.scientific.net/AMM.204-208.2236.

[5] Yan Yihang, Wu Dingjun, Li Qi. A three-dimensional method for the simulation of temperature fields induced by solar radiation. Advances in Structural Engineering, 2019, 22(3): 567-580. DOI: 10.1177/1369433218795254.

[6] Hu Lihua, Li Dejian, Chen Jianping, et al. Thermal effect analysis of skewed high piers of long-span continuous box girder bridge under sunshine temperature. Journal of Railway Science and Engineering, 2013, 10(2): 23-29. DOI: 10.19713/j.cnki.43-1423/u.2013.02.005.

[7] Hossain Tanvir, Segura Seth, Okeil Ayman M. Structural effects of temperature gradient on a continuous prestressed concrete girder bridge: analysis and field measurements. Structure and Infrastructure Engineering, 2020, 16(11): 1539-1550. DOI: 10.1080/15732479.2020.1713167.

[8] Gu Bin, Zhou Fengyuan, Gao Wanyang, et al. Temperature gradient and its effect on long-span prestressed concrete box girder bridge. Advances in Civil Engineering, 2020: 1-18. DOI: 10.1155/2020/5956264.

[9] Wu Jinwen. Application of structural health monitoring system on Poyang Lake Bridge. Proceedings of the 11th Annual Academic Conference of the China Highway Society Maintenance and Management Branch. Nanjing, Jiangsu, China, 2021: 435-440. DOI: 10.26914/c.cnkihy.2021.002652.
[10] Liang Zhu, Zhang Gejun, Li Na. Temperature test and analysis of steel box girder structure. Journal of China & Foreign Highway, 2009, 29(6): 126-128. DOI: 10.14048/j.issn.1671-2579.2009.06.039.
[11] Gou Hongye, Chen Zihao, Liu Chang, et al. Temperature field study of composite girder-bridge ballastless track system on arch in high-altitude large daily temperature difference region based on measured data. Journal of the China Railway Society, 2024, 46(2): 159-170.
[12] Liu Cheng. Temperature field and thermal effect study of steel-concrete composite bridges. Beijing: Tsinghua University, 2018. DOI: 10.27266/d.cnki.gqhau.2018.000059.
[13] Chen Yuwei, Chen Jianbing, Zhou Chen, Zhai Musai. Temperature effect study of steel-concrete joint section of wide hybrid girder cable-stayed bridge. Journal of Wuhan University of Technology (Transportation Science & Engineering), 2024, 48(5): 969-973.
[14] Xu Yan. Temperature effect study of hybrid girder cable-stayed bridge with single tower. Chongqing: Chongqing Jiaotong University, 2022. DOI: 10.27671/d.cnki.gcjtc.2022.000528.
[15] Zhang Xiangming, Li Chang, Guo Hanshu, et al. T Temperature effect study of wide hybrid girder cable-stayed bridge with high and low towers. World Bridges, 2026: 1-8.
[16] Huang Wenqiang, Xue Xiaoqiang, Xu Song, et al. Study on influence of temperature on mid-span vertical displacement of cable-stayed bridge with high and low towers. Anhui Architecture, 2023, 30(10): 154-156. DOI: 10.16330/j.cnki.1007-7359.2023.10.061.